Impact of substrate diffusion and enzyme distribution in 3D-porous electrodes: a combined electrochemical and modelling study of a thermostable H 2 /O 2 enzymatic fuel cell

Ievgen Mazurenko, Karen Monsalve, Pascale Infossi, Marie-Thérèse Giudici-Orticoni, Frédéric Topin, Nicolas Mano, Elisabeth Lojou

Impact of Substrate Diffusion and Enzyme Distribution in 3D-Porous Electrodes: a combined electrochemical and modelling study of a thermostable H_2/O_2 Enzymatic Fuel Cell

Ievgen Mazurenko,[a] * Karen Monsalve,[a] Pascale Infossi,[a] Marie-Thérèse Giudici-Orticoni,[a] Frédéric Topin,[b] Nicolas Mano,[c] Elisabeth Lojou [a] *

[a] Aix Marseille Univ, CNRS, BIP, 31 chemin Aiguier, 13402 Marseille, France

[b] Aix-Marseille Univ, IUSTI-CNRS UMR 7343, Technopôle de Château Gombert, 5, Rue Enrico Fermi, Marseille Cedex 13 13453, France

[c] Centre de Recherche Paul Pascal, UPR 8641, CNRS, Bordeaux University, 33600 Pessac, France

* Corresponding authors: lojou@imm.cnrs.fr, imazurenko@imm.cnrs.fr

Abstract

Using redox enzymes as biocatalysts in fuel cells is an attractive strategy for sustainable energy production. Once hydrogenase for H_2 oxidation and bilirubin oxidase (BOD) for O_2 reduction have been wired on electrodes, the enzymatic fuel cell (EFC) thus built is expected to provide sufficient energy to power small electronic devices, while overcoming the issues associated with scarcity, price and inhibition of platinum based catalysts. Despite recent improvements, these biodevices suffer from moderate power output and low stability. In this work, we demonstrate how substrate diffusion and enzyme distribution in the bioelectrodes control EFC performance. A new EFC was built by immobilizing two thermostable enzymes in hierarchical carbon felt modified by carbon nanotubes. This device displayed very high power and stability, producing 15.8 mWh of energy after 17 h of continuous operation. Despite large available electrode porosity, mass transfer was shown to limit the performance. To determine the optimal geometry of the EFC, a numerical model was established, based on a finite element method (FEM). This model allowed an optimal electrode thickness of less than 100 μm to be determined, with a porosity of 60%. Thanks to very efficient enzyme wiring and high enzyme loading, non-catalytic signals for both enzymes were detected and quantified, enabling the electroactive enzyme distribution in the porous electrode to

be fully determined for the first time. High total turnover numbers, approaching 10^7 for BOD and 10^8 for hydrogenase, were found, as was an impressive massic activity of 1 A mg^{-1} with respect to the mass of the electroactive enzyme molecules. The strategy, relying on stable enzymes and mesoporous materials, and the model set up may constitute the basis for a larger panel of bioelectrodes and EFCs.

Broader context

The transition to intrinsically intermittent renewable energy sources implies the storage of the excess energy produced and its retrieval upon demand. Hydrogen is a promising candidate as an energy carrier that can be converted to electricity in fuel cells. The sustainability of fuel cells relies, however, on the replacement of the scarce and expensive noble metal catalysts that are currently used. Efficient, specific redox enzymes, such as hydrogenases and multicopper oxidases, for H_2 oxidation and O_2 reduction into water appear as promising alternative biocatalysts in the enzymatic fuel cells thus built. To make the leap towards any industrial development, scale-up is now required, while maintaining high activity of the enzymes, hence high power output, and decreasing the amount of enzymes as far as possible to minimize the industrial cost. Depending on the application in which the biofuel cells are involved, stability of the biodevices may also be an issue. Here, we present a unique combination of thermostable enzymes entrapped in hierarchic porous carbon felts and numerical modelling of bioelectrodes to design a noble-metal-free fuel cell delivering stable, high power over a large range of temperatures. High massic activity of the biocatalyst makes our bioelectrodes competitive with the target defined by the U.S. Department of Energy by 2020. Beyond the H_2/O_2 enzymatic fuel cell domain, the strategies set out in this work offers great opportunities for the exploration of other redox enzyme-based biodevices in connection with environmental concerns (CO_2 reduction, N_2 conversion, water splitting, etc.).

Introduction

Enzymes are extremely active, regulated and specific catalysts designed by nature over billions of years of evolution from abundant elements. In the context of the approaching global energy crisis and the environmental worries raised notably during COP21, reducing our dependence on fossil

fuels and switching to renewable energy sources in the framework of bioeconomy development has become an extremely urgent issue. This implies that special attention should be paid to processes such as solar water splitting, carbon dioxide fixation and non-fossil fuel conversion, i.e. domains where the application of bioavailable and biodegradable enzymes could greatly enhance catalysis performance and sustainability. On the one hand, despite their structural complexity, enzymes can be easily produced in bacteria, which can be considered as nature's factories. On the other hand, recent developments in genetic engineering and our knowledge of the extraordinary biodiversity of living organisms, now make it possible to design or to purify enzymes able to operate in a variety of conditions, including extreme ones, notably at temperatures close to the boiling point of water. Such thermostable enzymes are also likely to be more stable and more resistant than their mesophilic homologues at room temperature, thus opening up new avenues to resolve the intrinsic instability of biocatalysts.[1]

The emergence of renewable energy also requires the use of reliable energy carriers, needed to transfer the energy to a final consumer. Provided a clean and renewable means of production is available, hydrogen may act as a green energy carrier, which can be transported to the consumption destination and converted to electrical energy and water upon reaction with atmospheric oxygen in fuel cells. Various redox enzymes, in which only abundant elements serve as catalytic sites, can advantageously replace platinum group metals in the design of H_2/O_2 enzymatic fuel cells (EFC). This is notably the case of hydrogenases and multicopper oxidases such as bilirubin oxidases, whose activity for hydrogen oxidation or oxygen reduction is several times higher than that of a platinum catalytic cluster. However, EFC industrialization relies on the ability both to produce enzymes at low cost and to attain high efficiency of the biocatalyst in the immobilized state. Ways to minimize enzyme loading and maximize their involvement in the catalysis must therefore be sought. The small volumetric activity of these large enzymatic molecules, and the insulation of the redox active sites in the protein shell impose rational strategies for electrically wiring the enzymes on the conductive materials.

One more issue associated with H_2/O_2 EFCs is linked to the sensitivity to oxygen of the anode enzyme, the hydrogenase, and explains why such EFCs are still considered as emerging devices compared to sugar/O_2 analogues.[2] Nevertheless, fast improvement has been reported in H_2/O_2 EFCs during the last few years and the power they can deliver allows applications to be envisioned in small portable electronic devices.[3,4] This is primarily due to the identification of O_2-tolerant hydrogenases in the biodiversity of microorganisms, such as hydrogenases from *Escherichia coli*,[5] *Ralstonia eutropha* [6] or *Aquifex aeolicus* (*Aa* MBH) [7]. It is also linked to two main strategies developed for the efficient immobilization of the enzymes on the electrochemical interfaces. The first is based

on enzyme entrapment in redox hydrogels.[8] This strategy, developed some time ago for O_2 reduction and sugar oxidation[9], has been successfully adapted to H_2 oxidation by hydrogenases. Not only does the mechanism of electron hopping between the redox entities in the redox polymer remove, a priori, the need for the enzymes to be oriented for electrical wiring, but the viologen-based polymer has also been demonstrated to act as a barrier against oxidative damage of the hydrogenase. Even hydrogenases recognized to be strongly inhibited by O_2 are then usable in EFCs. One drawback of this method is the limited amount of enzymes effectively contributing to the current, which means that power densities are limited to about 0.2 mW cm^{-2}.[8,10,11] The second strategy is based on the use of conductive materials with a high surface area/volume ratio to increase the loading of wired enzymes. Suitable functionalization of the material can enhance the direct interfacial electron transfer (DET) rate by placing the available surface electronic relay on the enzyme surface at a small distance from the material. Thus, Kano and co-workers immobilized the enzymes in functionalized Ketjen black films arranged as a gas diffusion electrode (GDL).[12] High power densities, of more than 5 $mW.cm^{-2}$, were reached thanks to the combination of high loading of wired enzymes and high feeding of H_2 and O_2 through the GDL electrodes.[13] However, no information on the stability of the device was provided, which raises questions for enzymes maintained in the unfriendly environment of GDLs. The Armstrong group reported the entrapment of enzymes in a compacted film of graphite, and designed membrane-less H_2/O_2 EFCs delivering more than 1 mW that were thus able to power a LED for 8 h with no decrease in the light intensity.[4] Our group designed an EFC based on enzyme immobilization in macroporous carbon felts able to power a wireless electronic device sending 5 different data every 25 s for 7 h.[3] We also designed a preliminary H_2/O_2 EFC able to operate in a range of temperatures from 25 to 70°C thanks to the immobilization on thin films of carbon nanofibres of two thermostable enzymes, *i.e. Aa* MBH O_2-tolerant membrane-bound hydrogenase for H_2 oxidation and bilirubin oxidase from *Bacillus pumilus* (*Bp* BOD) for O_2 reduction.[14] More recently, we determined the most suitable surface chemistry of carbon nanotubes to enhance bioelectrocatalysis using *Aa* MbH[15] and *Bp* BOD. We especially demonstrated that carbon nanotubes functionalized by amino-pyrene derivatives favoured a preferential orientation of the enzymes for direct, efficient electrical wiring.[16,17]

Despite these advanced performances, many factors that limit such biodevices in terms of power output and stability remain largely unknown. This is particularly true for the fraction of enzymes effectively participating in biocatalysis in carbon nanomaterials. Two usually unknown variables influence this amount. The first is the quantity of active enzyme molecules actually contacting and exchanging electrons with the electrode surface. Being determined from non-catalytic signals for

molecular catalysts, these data are lacking for multicentre redox enzymes such as hydrogenase, which precludes any quantitative determination of the turnover of immobilized enzymes and catalyst specific current densities.[18] The second unknown variable is the amount of enzymes that experience conditions of sufficient substrate supply to perform their catalytic functions. Mass transport of substrates is expected to play a key role, especially when the low solubility of gases in the aqueous phase is considered. Given the complex enzymatic substrate- and potential-dependent kinetics, it appears hardly feasible to experimentally investigate all the interrelated parameters that could affect the EFC. If devices beyond laboratory prototypes are to be achieved, modelling is required for in-depth investigation of the overall operation of the EFC and for characterization of the bioelectrodes at the molecular level.[19]

The purpose of this work is to analyse the influence of mass transfer and enzyme loading and distribution on the performance of DET-based porous bioelectrodes using the relevant example of a thermostable H_2/O_2 EFC. With this aim, we first design a new type of H_2/O_2 EFC by combining the advanced aspects of the bioelectrodes developed in our previous works: use of macroporous carbon felt modified by aminomethylpyrene-functionalized carbon nanotubes to entrap two thermostable enzymes, *Aa* MBH and *Bp* BOD. An analysis of the performances of this EFC in terms of power and stability as a function of parameters such as temperature and substrate supply, highlights mass transfer as the main limitation. We set a model of mass and charge transport in porous media. The balance equations are numerically solved using commercial software based on finite element method (FEM) that is well suited for this kind of diffusion-reaction set of equations in complex geometries. This tool allows to determine the optimal geometry of the EFC, and permits a comprehensive study of the substrate diffusion inside the porous bioelectrodes, with special focus on the effects of the thickness and porosity. The wired enzyme distribution is then elucidated as a second main factor that could affect EFC performance. We show that the hierarchical porous structure and functionalization of the carbon material is able to induce high wiring of enzymes. Hence non-catalytic signals are detected for BOD and, above all, for hydrogenase, for which this signature has been observed only twice. The analysis of the proportion of embedded enzymes participating in the catalysis highlights the extreme efficiency of the bioelectrodes designed in this work, which approach the efficiency of platinum. Finally, we discuss the potential prospects of porous bioelectrodes, notably in connection with catalyst protection against reactive oxygen species.

Methods

Materials

Membrane-bound [NiFe]-hydrogenase from *Aquifex aeolicus* (*Aa* MBH) was purified as described elsewhere.[20] Bilirubin oxidase from *Bacillus pumilus* (*Bp* BOD) was produced and purified as previously described.[21]

2,2'-azino-bis(3-ethylbenzothiazoline-6-sulfonic acid) (ABTS), N-Methyl-2-pyrrolidone (NMP), and dimethylformamide (DMF) were purchased from Sigma-Aldrich. 1-Pyrenemethylamine hydrochloride ($PyrNH_2$) was from Aldrich. Phosphate buffer solutions were prepared by mixing Na_2HPO_4 and NaH_2PO_4 to final buffer concentrations of 0.1 M or 0.2 M (PB).

Carbon felt (CF) RVC 2000 (thickness 6 mm) was purchased from Mersen. Multiwalled carbon nanotubes (CNTs) (NC3100™, 1.5 μm × 9.5 nm, >95% purity) produced by catalytic chemical vapour deposition (CCVD) were obtained from Nanocyl SA (Belgium). CNT suspensions (1 mg mL^{-1}) were prepared by sonication in NMP for 4 h. These suspensions were centrifuged at 13 000 rpm for 2 min and the supernatant was used for electrode modification.

Electrode preparation

Cylinders with a diameter of 5 mm (external surface area 1.34 cm^2) cut from the CF-carpet were washed with ethanol, dried and used as electrodes. A defined amount of the CNT suspension (135 μL) was injected into the CF-electrode and left to dry at 80 °C in air for 24 hours (similar results were obtained with drying under vacuum). This procedure was repeated several times in order to obtain the desired number of CNT-layers (a maximum of 12 layers were used in this work). The as-prepared electrodes (designated as CF-CNT) were stored in a closed flask at room temperature. For the sake of comparison, a planar pyrolytic graphite (PG) electrode (d = 5 mm) was modified with 3 layers of CNTs by dropping 3 x 5 μL of CNT-dispersion on the electrode and letting it dry at 80 °C.

Before enzyme immobilization, CF-CNTs were modified by π-π stacking with $PyrNH_2$ by immersing them in 20 mM $PyrNH_2$ solution in DMF for 8 hours at 4 °C. The resulting electrodes were thoroughly washed with water and connected in the wetted state to a rotating electrode system with a graphite needle. The enzyme immobilization was carried out at 25 °C in 10 mL of 0.2 M PB solution (pH 7 for *Aa* MBH and pH 6 for *Bp* BOD), with the CF-CNT rotating at 1000 rpm, by adding defined amounts of *Aa* MBH or *Bp* BOD. Catalytic curves in the presence of the corresponding substrates were recorded during enzyme adsorption until equilibrium was established. Afterwards, the electrodes were transferred to the enzyme-free solutions or to the

compartments of the EFC (in the latter case the solution pH was changed from 7 to 6 for the bioanode).

Techniques

The electrochemical measurements (cyclic voltammetry (CV), chronoamperometry (CA) and square-wave voltammetry (SWV)) for a single bioelectrode were performed in a standard 3-electrode cell comprising a modified CF-CNT, an Ag/AgCl (sat. NaCl) or Hg/Hg_2SO_4 reference electrode and a Pt-wire auxiliary electrode. All the potentials were recalculated and referred to an Ag/AgCl reference electrode. The cell was sealed, thermostated and controlled by an Autolab M101 (Metrohm, Switzerland) potentiostat. Depending on the needs of the experiment, hydrogen, nitrogen or oxygen were constantly circulated through or above the solution. Before enzyme immobilization, the electrode capacitance was measured by performing a CV in the range 0.1− 0.4 V and retrieving the charging current at different scan rates from 35 to 350 mV s^{-1}. The value of the capacitance was determined as the slope of the current versus scan rate dependence and was used to estimate the electroactive surface area of the CF-CNTs, assuming an average specific capacitance value of 10 μF cm^{-2} for carbon materials (from 5 to 25 μF cm^{-2}, 3 μF cm^{-2} for basal plane carbon).[22]

In the membrane fuel cell configuration, two water-jacket beakers of approximately 150 mL volume separated by a 4 cm diameter Nafion membrane (0.18 mm, Alfa Aesar) were used as anodic and cathodic compartments and fed with pure H_2 or O_2 respectively. Corresponding CF-electrodes attached to the rotating electrode were placed in each compartment, and were thus 11.5 cm apart. An auxiliary electrode, a reference electrode and a gas bubbler were also placed in each compartment.

Nitrogen adsorption isotherms were determined at 77 K on the Micromeritics ASAP 2020 on samples that had been treated at 393 K under vacuum overnight. When hysteresis was present in the mesoporous range, the mesopore size distribution was calculated from the desorption branch at $p/p_0 > 0.4$ using the Barrett-Joyner-Halenda (BJH) method.[23] Mercury porosimetry was performed using a Quantachrome Poremaster 60 apparatus by applying pressures from 0.2 to 54000 psi. The resulting curve was analysed by Washburn's equation considering the cylindrical shape of the pores.[24]

Scanning electronic microscopy images (SEM) were acquired using a Tescan Vega 3 apparatus with a secondary electron detector and an acceleration voltage of 20 kV.

Enzyme solution properties

In order to construct a mathematical model, the apparent Michaelis constants (K'_m) of both enzymes for substrate conversion were needed. The K'_m of *Aa* MBH had been previously estimated to be as low as 3 μM.[17] The K'_m of *Bp* BOD is unknown and its value was determined electrochemically by varying the O_2 concentration and following the catalytic current with *Bp* BOD immobilized on PG-CNT at different rotation rates and different potentials (Figure S1A). The Koutecky-Levich plot was then used to approximate the catalytic current at infinite rotation rate, followed by fitting to the Michaelis-Menten equation. The K'_m value of 37±3 μM was found at all potentials lower than 0.35 V, at pH 6 and 25 °C (Figure S1B-D).

Bp BOD enzymatic activity was measured by UV-Vis spectroscopy at 30 °C in 0.1 M phosphate-citrate buffer pH 4 in the presence of ABTS. The catalytic reaction was followed at 420 nm ($\varepsilon = 3.6 \times 10^4$ M^{-1} cm^{-1}). *Aa* MBH activity was measured by UV-Vis spectroscopy at 60 °C in 0.05 M HEPES buffer pH 7 in the presence of Methylene Blue. The solution was saturated with hydrogen and the decrease of the adsorption at 550 nm ($\varepsilon = 6.19 \times 10^3$ M^{-1} cm^{-1}) was followed. All turnover constants in the text are defined as the number of H_2 or O_2 molecules oxidized or reduced per second by one molecule of the corresponding enzyme.

The equilibrium concentration of enzyme in the cell during the adsorption step on the electrodes was found to be rather small at the initial stage of the isotherm (nM range). The direct methods of enzyme concentration determination (Lowry, Bradford, etc.) could not be applied without time-consuming and error-prone preconcentration steps. Thus, the corresponding enzymatic activity in the cell was measured indirectly by UV-Vis spectroscopy and correlated with the enzymatic activity of the initial enzyme solution of a known concentration. In this case, 100 μL of the cell solution was taken out and its activity was measured as mentioned above. The value was then compared with the activity of the stock enzyme solution at a concentration of 50 nM in order to deduce the equilibrium concentration of the corresponding enzyme in the cell. The amount of enzyme adsorbed on the electrode was then calculated by subtracting the equilibrium (non-adsorbed) enzyme quantity from the total enzyme amount added into the cell.

Modelling

A 3D-model of the electrochemical cell was created to study the substrate diffusion of each bioelectrode separately. In addition, a 2D-model was used to evaluate the performance of both electrodes in optimal fuel cell configuration. In both cases, the models included enzymatic kinetics as a function of applied potential and substrate concentration, mass-transfer of the substrate,

solution resistivity and the influence of electrode porosity on the apparent diffusion coefficients and solution conductivity. The resulting set of equations was solved using finite-element method implemented in the Comsol Multiphysics® 5.2a package. The model is described in detail in the Supporting information (Figures S2-S7).

Results and discussion

Functionalized carbon felt properties

The CF electrodes used in this study as conducting macroporous scaffolds consisted of large 10 μm diameter fibres forming an interconnected network with an interfibre distance of approximately 50 μm (Figure S8A). The porosity of the CF determined by mercury intrusion was found to be about 90% (cumulative volume of pores 8.5 cm^3 g^{-1}), i.e. no significant hindering of species diffusion was expected inside of the electrode (Figure S8B). No significant pore volume was found below 20 μm, suggesting a low specific surface area. Hence, CF alone did not allow high amounts of enzymes to be adsorbed and this resulted in moderate current densities as shown previously for *Aa* MBH and *Myrothecium verrucaria* BOD.[3] Therefore, additional CF modification by CNTs was performed in order to increase its specific surface area and to create mesoporosity suitable for enzyme adsorption.

The hydrophobicity and high aspect ratio of the pristine CNTs allowed them to adhere strongly to hydrophobic surfaces and was used to perform the CF modification using a Layer-by-Layer approach. Upon solvent evaporation, the CNTs deposited on the CF fibres were not redispersed when a new portion of the solvent was added. No macropore clogging was observed and homogeneous covering of the fibre surface by the CNTs can be clearly seen in the SEM image at high magnification (Figure 1A). The quantity of deposited CNTs scaled almost linearly with the number of layers deposited as evidenced by the CF-CNT capacitance measurements during the deposition (Figure S8C). Thus, the specific electroactive surface area increased from 0.2 to 2.9 m^2 g^{-1}, i.e. 15 times, upon deposition of 12 CNT layers. At the same time, the final mass ratio of CNTs in the CF-CNT was approximately 4 %, which corresponds to a negligible decrease of the apparent porosity considering the CNT density of 2.6 g cm^{-3}.

Nitrogen adsorption isotherms for both non-modified and CNT-modified CF are shown in Figure 1B. The CF-CNT presents a type IV isotherm with hysteresis clearly visible at high partial pressures, suggesting the presence of mesopores (inter-tube voids of the CNT-network) in which capillary condensation occurs. Within its applicability limits, the Barrett-Joyner-Halenda theory was

used to estimate the mesopore size distribution. A major contribution of the pores between 10 and 40 nm was found (Figure 1B, inset). Hence, CF modified by CNTs provides a hierarchical porosity. It has mesopores close to the enzyme size, which are thus suitable for enzyme entrapment,[25] while keeping high macroporosity favourable for substrate diffusion. Taking this fact and posterior CNT modification by Pyr-NH_2 into account, CF-CNT should constitute a suitable matrix for both *Aa* MBH and *Bp* BOD immobilization in terms of enzyme loading and DET-connection.

H_2/O_2 EFC assembly: performances and limitations

The modified bioanode and biocathode were first evaluated separately at a constant rotation speed of 1000 rpm. The CVs of both electrodes in the presence of the substrates revealed characteristic catalytic currents of H_2 oxidation and O_2 reduction by the respective enzymes with onsets at -0.5 V and 0.5 V for the anode and cathode, respectively (Figure 2A). In both cases, the catalytic currents were enhanced with increasing temperature, although the slope of the increase was steeper for *Aa* MBH than for *Bp* BOD (3.2-fold against 1.8-fold increase when the temperature was raised from 25 to 50 °C (Figure 2A). This fits well with the hyperthermophilic nature of *Aquifex aeolicus*, which thrives at temperatures as high as 85 °C, while *Bacillus pumilus* is a mesophilic bacterium with optimal growth rate at 30-40 °C but is able to form spores that resist higher temperatures.[26] At the maximum currents, the catalytic-to-capacitive current ratio was in the order of 1000 at 5 mV s^{-1} for *Bp* BOD and *Aa* MBH. This argues for a high ratio of DET-orientated enzymes and an efficient surface utilization due to the preliminary surface modification by PyrNH_2. The absolute currents achieved separately with anode and cathode and their normalized values are summarized in Table 1. They reach high values, between 6 and 27 mA, according to the temperature. In the case of porous 3D electrodes, it is always difficult to calculate current densities since they depend on the surface area that is taken into account. In the present case, current densities ranging from 5 (25 °C) to 16 (50 °C) mA cm^{-2} and from 12 (25 °C) to 20 (50 °C) mA cm^{-2} were obtained for *Aa* MBH and *Bp* BOD respectively when the external surface area of the cylindrical electrode was considered (Table 1). These values exceed the performances of the most recently developed H_2/O_2 EFCs except those based on gas-diffusion systems (Table 2). The volumetric current densities ranged from 55 (25 °C) to 180 (50 °C) mA cm^{-3} and from 135 (25 °C) to 231 (50 °C) mA cm^{-3} for *Aa* MBH and *Bp* BOD respectively.

The effect of the rotation rate on the biocatalysis was studied for the bioanode and biocathode at different temperatures (Figure S9). Up to 30 °C, the hydrogen oxidation current did not vary with the rotation rate above 1000 rpm, but a catalytic current decrease and a characteristic plateau were

observed at lower rotation rates, suggesting hydrogen depletion and mass-transfer controlled current (Figure S9A). As the temperature increased, the hydrogenase activity and therefore the volumetric rate of hydrogen consumption also increased. Consequently, higher rotation rates were needed to counterbalance hydrogen consumption. (Figure S9A). A similar situation was observed for *Bp* BOD modified electrode (Figure S9B). In both cases, the catalytic currents did not follow the Levich equation at all temperatures and displayed saturation at high rotation rates (Figure S10). Similar behavior has already been observed for 3D electrodes and was connected to different rates of solution penetration inside a porous electrode. [27,28]

The EFC built with the above bioelectrodes presented an OCV of 1.02 V at 25 °C. Figure 2B shows the polarization curves of the EFC obtained in the galvanostatic mode. A maximum power ranging from 1.3 at 25 °C to 2.3 mW at 50 °C was obtained, corresponding to high power densities of 1.0 mW cm^{-2} at 25 °C and 1.7 mW cm^{-2} at 50 °C (Table 1). The fully assembled EFC was subjected to a galvanostatic stability test (Figure 2C). When a 1.5 mA current was applied, the EFC demonstrated excellent stability, displaying only 5 % power loss during 17 hours of operation at 25 °C, thus producing 15.8 mWh of electrical energy. The OCV observed after the circuit was opened was only 17 mV lower than the initial one. These performance levels, in terms of both power output and stability, place our H_2/O_2 EFC in the highest range ever reported, with an additional advantage of operating at a range of temperatures between 25 and 50 °C.

To evaluate the effect of mass transfer on the EFC performances, the polarization curves at 25 and 40 °C were repeated in the absence of any convection, i.e. mass-transfer was governed exclusively by diffusion (Figure 2D). As expected from the behaviour of each bioelectrode described before, drastically lower maximum power was obtained in these conditions. It was around 130 and 150 μW at 25 and 40 °C, which corresponds to 10 % and 8 % respectively of the power obtained in the same conditions but with electrode rotation. Maximum currents in the order of 200 μA could be sustained by the anode. Further current increase drove the anode potential to sufficiently high values for rapid classical anaerobic deactivation of *Aa* MBH to occur.[29] The lower power and current obtained in this condition are again indicative of substrate depletion due to the enzymatic reactions inside the 3D electrode. Moreover, the hydrogen scarcity inside the CF increases the apparent deactivation rate of hydrogenases.[29] Mass-transfer thus appears as a major parameter affecting the performance of the H_2/O_2 EFC based on porous enzyme electrodes.

Bioelectrode modelling

In order to study the issue of substrate depletion in detail and to determine the optimal bioelectrode geometry, FEM modelling of substrate diffusion was performed. First, a 3D-model was constructed of the CF-electrode and a part of the cell in the 3-electrode configuration (Figure 3A). In this model, the Fick's second law equation and the solution current distribution were coupled to the mass-sink inside the CF-domain as a function of applied potential and substrate concentration according to Michaelis-Menten kinetics. The decrease of substrate diffusion rate inside the porous electrode was based on the tortuosity model and the Bruggeman equation connecting porosity and tortuosity (SI Model description). The following assumptions and simplifications were also made: a) *Aa* MBH high potential deactivation was excluded from the model since its exact potential and substrate dependence is unknown; b) the pH of the solution did not vary (buffered electrolyte); c) the electrode resistivity was negligible; d) substrate mass-transfer occurred solely as a result of diffusion, with no migration or convection contributions; e) the CF-electrode and the enzyme distribution within the CF were homogeneous.

The potential-dependent enzyme kinetics was deduced from the experimental curves at 4000 rpm (Figure 3B, C, black lines), i.e. in the conditions of sufficient substrate supply, and corrected for ohmic drop (SI Model description). The model was then verified by simulating CVs in the absence of rotation. Figure 3B, C shows the real (red lines) and simulated (blue lines) voltammetry curves at 5 mV s^{-1} and stationary conditions for the bioanode and biocathode respectively. The simulated curves represent the shape of real curves well despite the simplifications of the model mentioned above. The biggest discrepancy between simulated and experimental CVs for both bioelectrodes is observed in the region of the current drop due to the substrate depletion in the CF-volume. In this case the slope of the current decrease is much steeper for the simulated curve. This can be explained by the homogenization of the CF-domain in the model, i.e. the substrate is consumed evenly throughout the CF-domain, although only fibre surfaces covered by CNTs are active in reality. Consequently, substrate would have to diffuse over the inter-fibre distance (several tens of μm) first in order to react. This diffusion time is not included in the model but it influences such dynamic methods as CV, leading to a steeper slope of the current decrease in the simulated curves in comparison with experimental ones. The precise morphology of the CF should be taken into account on the macroscopic level to build a more realistic model. However, the resulting significant bias is expected only in the case of a fast dynamic transition and should be less pronounced for stationary conditions.

The spatial substrate concentration distribution inside the CF is shown in Figure 3D, E as a function of the applied potential during a CV scan at 5 mV s^{-1}. In both cases, the substrate concentration inside the porous electrode drops rapidly to almost zero as the scan proceeds. At

potentials close to 0 V, only the external layer of the CF-CNT, less than 0.5 mm thick, is provided with substrate by diffusion from the external solution, although its concentration is less than 5% of the initial one. The substrate starts to penetrate into the CF-CNT again when the applied potential returns to values where the reaction rate is slow. The maximum ohmic drop inside CF-CNT does not exceed 25 mV and rapidly diminishes to a negligible level as soon as the current of the bioelectrode decreases to mass-transfer limited values. Substrate mass-transfer as a major limiting factor of the EFC in the absence of forced convection is thus confirmed by our FEM modelling.

Considering the substrate distribution during the operation, it seems obvious that, in the diffusion-controlled mass-transfer mode, the thickness of the porous electrode can be significantly reduced without any loss in current densities. The simulation can be further used to deduce the optimal configuration of the bioelectrodes and to estimate the performance of an H_2-air EFC in such a configuration. Intuitively, the gaseous phase (H_2 or air), in which the magnitudes of both diffusivity and substrate concentration are 3-4 orders of magnitude higher than in the liquid phase, should be brought as close as possible to the porous electrode in order to provide maximum substrate flux. The 2D model assuming 1 cm^2 bioelectrodes with previously defined enzyme volumetric kinetics and with different thicknesses was built and stationary polarization curves were simulated in the absence of forced convection (Figure 4A, Figure S5). Figure 4B shows the variation of maximum current and power densities of the EFC for the anode and cathode, obtained at different thicknesses. It appears that making the developed bioelectrode thicker than about 250 μm no longer leads to enhanced EFC-performance as the substrate is consumed faster than it penetrates inside the electrode. Moreover, a slight decrease of current and power densities is observed for thicker electrodes as a result of electrolyte resistivity. Furthermore, we performed a simple simulation of the influence of porosity by taking advantage of the flexible nature of the CF-CNT. CF-CNT can easily be compressed several times thus bringing more catalysts close to the gas phase boundary, but also decreasing the porosity and substrate diffusivity (See explanation in SI). The effect of such compression is shown in Figure 4C. Compressing 4 times, i.e. decreasing the porosity from 0.9 to 0.6 produces maximum current density of 1.3 mA cm^{-2} and maximum power density of 0.5 mW cm^{-2} for the modelled EFC. With further compression, the porosity, and thus the apparent diffusion coefficient, become too low, leading to marked substrate diffusion and current flow limitation. A similar effect is predicted from the increase of the quantity of CNT deposited, and hence the amount of enzyme adsorbed. However, in this case it is difficult to estimate the corresponding tortuosity change with CNT deposition, and more precise modelling of the substrate diffusion and reaction is needed according to the microscopic shape of the pores.

The EFC performances modelled are in line with those of other up-to-date devices developed in the "classical" fuel cell configuration, in which the bioelectrodes are completely in the liquid phase, although the gas bubbling used in most of the cases is likely to induce some additional convection and substrate supply (Table 2). The substrate availability being the major limiting factor, gas-diffusion systems can be a solution offering a ramified three-phase boundary and providing large substrate flux. The latest developments of enzymatic gas-diffusion systems show geometric current and power densities an order of magnitude higher (Table 2). The long-term operational stability of such systems has not been evaluated, however. Being biological catalysts, enzymes habitually operate in the liquid phase and even a short contact with a gaseous phase and drying can be harmful for the biomolecule. In our conditions, the liquid phase and the appropriate porosity of the CF-CNT, where the enzyme is adsorbed in a confined environment, may, on the contrary, provide a friendly environment and enhance the stability of the biomolecules.

3D porous materials for biocatalyst protection?

Whether the porous matrix may help in overcoming the instability of EFCs induced by the use of biological catalysts, which prevents their industrial application, is currently an open question. This could be even more critical for devices based on metalloenzymes, which contain many cofactors and are recognized as fragile catalysts. We have demonstrated above the stability of the EFC based on *Aa* MBH and *Bp* BOD adsorbed in CF-CNT (Figure 2C). More insights into the role of the porous matrix can be obtained by analysing each bioelectrode separately.

The *Bp* BOD modified CF-CNT demonstrated only a 30% decrease of the catalytic current in 90 hours of continuous operation in the potentiostatic mode in oxygen-saturated conditions and at room temperature (Figure S11A). It should be noted that the electrode was rotating at 1000 rpm and no mass-transfer limitations were expected at such current. This means that the catalytic current decrease indeed corresponded to the enzyme deactivation/denaturation. In such cases and at a fixed potential, the enzyme deactivation kinetics is often of first order and can be described using an exponential decay equation.[30] The immobilized *Bp* BOD half-life at 25 °C estimated from a monoexponential fit was approximately 7 days, demonstrating that CF-CNT provides a friendly host-matrix for this enzyme immobilization.

Even better activity was demonstrated using CF-CNT modified by *Aa* MBH. In similar conditions to those used for *Bp* BOD, the bioanode had lost only about 14% of activity after operating continuously for 6 days (Figure S11B). The half-life of immobilized *Aa* MBH estimated from a

monoexponential fit was about 27 days at 25 °C. We believe that such excellent stability of the bioelectrodes is principally linked to the thermostable nature of both enzymes (even hyperthermostable in the case of *Aa* MBH), which usually possess a more robust structure than mesophilic enzymes thus slowing down the rate of denaturation. However, the porous matrix should also play a major role by protecting enzyme molecules that are confined in pores of suitable size.

Taking into account the general susceptibility of hydrogenases to oxygen,[11] the great stability of *Aa* MBH in the CF-CNT suggests that the use of 3D porous electrodes can also be advantageous for the protection of sensitive catalysts, especially in oxidative conditions. Earlier, Armstrong's group demonstrated the role of compacted carbon in protecting hydrogenases against oxygen, which was attributed to slower oxygen effusion inside the porous material.[4] In our case, the oxygen-tolerant nature of *Aa* MBH means that, a priori, it does not require protection against oxygen. This is shown by the fact that CF-CNT-*Aa* MBH can easily sustain a 100% O_2 atmosphere, losing only 1.3 % and 2.3 % of activity after 25 min and 60 min of exposure, respectively. (Figure 5A). However, we have shown recently that reactive oxygen species (ROS) formed as a result of oxygen reduction at carbon surface held at low potentials readily contribute to irreversible hydrogenase deactivation.[17] Accordingly, in this work, the bioanode lost almost 40% of its activity after 25 min exposure to pure O_2 at a reductive potential (Figure 5A). 3D porous matrix can be useful in such conditions for shielding the inner catalyst layer from the ROS, which would more probably react with the CNT-matrix before arriving at the catalyst layer.[31,32] Obviously, such protection is assumed to become more efficient as the thickness of the porous matrix and its specific surface area increase. As a demonstration, two electrodes with immobilized *Aa* MBH were prepared, the usual CF-CNT, and a PG-electrode covered with a CNT layer and $PyrNH_2$ (see experimental section). Both electrodes present similar surface chemistry but have different geometry, the former being a 3D electrode while the latter is a 2D one. Both electrodes, rotating at 1000 rpm, were then subjected to a constant applied potential of -0.4 V (vs. Ag/AgCl), i.e. a potential where significant oxygen reduction on the carbon surface occurred. The hydrogen oxidation current observed in such conditions was not high enough to be limited by substrate mass-transfer (yet more than 50-times higher for CF-CNT than PG-CNT) and was assumed to be proportional to the quantity of active enzymes. When the cell atmosphere was changed from 100% H_2 to a 93%H_2-7%O_2 mixture, a slight current drop, attributed to oxygen reduction, was observed (Figure 5B). Another possible reason could be *Aa* MBH deactivation by oxygen, but the low reductive potential at which the electrode was held was likely to reactivate *Aa* MBH.[7] Some ROS formed during oxygen reduction irreversibly deactivated *Aa* MBH and resulted in the decrease of the catalytic current when 100%

H_2 conditions were restored (Figure 5B). The proportion of destroyed enzymes was very different, however, for the 2D and 3D electrodes. While the 2D-electrode lost 3% and 13% of its activity after operating in the 93%H_2-7%O_2 mixture for 25 and 60 min respectively, the 3D-electrode was deactivated by less than 0.5% and 3% in the same conditions (Figure 5B). It should be noted that the amount of ROS generated is assumed to be about 50 times higher in the case of the 3D electrode, as can be deduced from the extent of the absolute oxygen reduction current. Despite such harsh conditions, *Aa* MBH encapsulated inside the 3D porous matrix seems to be 4-6 times more stable against ROS than when it is immobilized on the 2D electrode. The exact mechanism remains to be elucidated but, as discussed earlier, ROS are likely to be scavenged by the porous matrix before they arrive at the active catalyst layer, a behaviour similar to that described in redox hydrogels.[8,11] The protective nature of such porous electrodes should be further enhanced by making the surface more reactive towards ROS, thus opening up large avenues for further investigations. While being mostly relevant for hydrogenases, and even as demonstrated here for O_2-tolerant ones, this approach of ROS scavenging may be extended to any other enzymes facing O_2 in enzymatic biodevices and operating at low redox potentials – this is for instance the case of enzymatic H_2 production – where the possible ROS formation may have deleterious effect on the catalyst stability.[33]

Enzyme distribution in the porous 3D-electrode

The protective role of the porous matrix raises the additional question of the distribution of enzymes inside the material and, more particularly, of the distribution of the enzymes that effectively participate in the biocatalysis. The efficiency of future protection strategies will obviously depend on the way the enzyme distribution can be controlled in the porous matrix. Fortunately, the porous matrix presents a clear advantage in terms of enzyme loading, which has direct consequences not only on the level of the catalytic current but also on more fundamental issues related to the distribution of enzymes. The loading of enzyme, and especially the electroactive enzyme distribution, has, however, remained under-investigated, either because a homogeneous distribution is considered a priori, or because it is very difficult to access the accurate proportion of enzyme participating in the catalysis. The modification of CF with CNTs carried out in the present work increased its specific surface area by an order of magnitude while leaving its apparent porosity, i.e. species diffusivity, almost intact. The predominant formation of pores of size between 10 and 40 nm should be very suitable for the encapsulation of both *Bp* BOD and *Aa* MBH[25] implying a high enzyme loading. We performed enzyme quantification in order to confirm

this latter point and to determine the exact amount of electroactive enzymes participating in the catalysis.

Adsorption isotherms

Adsorption isotherms were first established by simple progressive adsorption from enzyme solution added into the electrochemical cell (Figure 6A, B). Because of the high material porosity and convection, a homogeneous enzyme distribution within the electrode volume was expected a priori. This was verified by cutting the CF-CNT into two unequal pieces and checking their respective catalytic responses as done previously for mesoporous carbon electrodes.[34] The catalytic curves of the initial electrode and of the two resulting pieces, normalized for the electroactive surface area of the respective electrodes, demonstrated good convergence, thus confirming the homogeneous distribution of the adsorbed enzymes (Figure S12).

The saturation of the catalytic signal occurred systematically at some point for both enzymes, and larger amounts of enzyme did not lead to further current increase. As the concept of DET precludes the electroactivity of enzyme molecules adsorbed farther than within a monolayer on the electrode, it seems obvious to ascribe the saturation to the completion of the enzyme monolayer on the electrode surface. Therefore, the enzyme adsorption should be sufficiently well described by Langmuir formalism, treating an idealized case of purely monolayer formation on a homogeneous surface:

$$\theta = \frac{q_{enz}}{q_{enz}^{max}} = \frac{K_L C_{enz}}{1 + K_L C_{enz}}$$

where θ is the fractional occupancy of adsorption sites,
q_{enz} and q^{max} are the actual and maximum amounts of enzyme molecules that can be adsorbed within a monolayer,
K_L is the Langmuir thermodynamic constant of adsorption,

and C_{enz} is the equilibrium concentration, i.e. the concentration of non-adsorbed enzyme molecules in the solution.

It should be noted that q and q_{max} depend on the electroactive surface area available for the adsorption and thus should be normalized. On the other hand, assuming the enzymes are adsorbed in the same orientation whatever the surface coverage, the adsorbed quantity is directly proportional to the catalytic current at a fixed potential. To support these assumptions, very similar

curves were obtained in different experiments with electrodes displaying various surface areas if both axes were normalized by surface area (example for *Aa* MBH in Figure S13). Yet, the fraction of the enzymes that is effectively adsorbed on the electrode remains unknown which does not allow establishing the real isotherms.

The indirect measurements of the remaining enzyme concentration in the cell after adsorption (see experimental part) allowed the adsorption isotherms to be established and the catalytic activity to be correlated with the quantity of enzymes adsorbed (Figure 6). The resulting isotherms (Figure 6C, D) show that the adsorption of both enzymes on CF-CNT was efficient: most of the added enzymes were effectively adsorbed on the electrode. Less than 10 nM stayed in the solution at the initial stage of the isotherms, despite 10-20 times more enzyme being added to the cell. This was also proved by the high values of the Langmuir constants - of the order of 10^8 M^{-1} - obtained after isotherm fitting (Table 3). An interesting result deduced from the isotherms was the maximum surface coverage, which was found to be 12.5±0.9 pmol cm^{-2} for *Bp* BOD and 2.7±0.2 pmol cm^{-2}, i.e. 4.5 times lower, for *Aa* MBH (Table 3). The crystallographic structures of both enzymes are still unresolved, but a rectangular footprint based on the homology modelling sequence can be estimated at around 30 nm^2 for *Bp* BOD and 83 nm^2 for *Aa* MBH (with the transmembrane helix), which correlates well with the ratio of maximum coverages for the two enzymes and proves the validity of the Langmuir approach for the enzymatic systems.

The apparent turnover constants calculated taking the catalytic current and the amount of adsorbed enzymes into account were 4±2 s^{-1} and 23±2 s^{-1} (at 0 V) for *Bp* BOD and *Aa* MBH respectively. These are notably smaller than those reported in solution-based assays (*Bp* BOD: 88 s^{-1} at 37°C with ABTS,[21] about 100-200 s^{-1} for O_2-tolerant hydrogenases[6]). Several reasons can be put forward to explain such a discrepancy: a decrease of enzyme efficiency upon immobilization, partial enzyme denaturation or incomplete electrical connection of enzymes.

Non-catalytic signal analysis

A decision on the importance of each of these possibilities required the recording of non-catalytic enzyme responses in order to calculate the exact number of enzyme molecules in direct electrical connection with the electrode. Detection of such signals for immobilized enzymes is tedious because of the large size of the enzymes and the presence of the insulating protein shell, which results in low surface coverage by electroactive molecules. This difficulty becomes more pronounced for larger enzyme molecules. While non-catalytic signals have been observed for several BODs,[35–37] they have been detected only once for [NiFe]-hydrogenase from *Chromatium vinosum*[38] and [NiFeSe]-hydrogenase from *Desulfomicrobium baculatum,*[39] and have never been seen for

O_2-tolerant membrane bound hydrogenases. In our system, the very high faradaic-to-capacitive current ratio observed in connection with the efficient surface modification by $PyrNH_2$ that allowed DET-orientation of enzyme molecules, could be expected to enhance the amount of wiring enzymes, thus offering the first opportunity to detect non-catalytic signals for both hydrogenase and BOD.

The amount of *Aa* MBH approximately corresponding to the inflection point of the adsorption isotherm was added and SWVs of CF-CNT-*Aa* MBH were recorded under a nitrogen atmosphere (Figure 7A). After enzyme addition to the electrolyte, the shape of the SWV started to evolve. Notably, peaks appeared at -0.45 V, -0.29 V and -0.07 V and grew with each SWV scan (315 s) until saturation was reached within about 1 hour (Figure 7A, coloured lines). The corresponding pairs of redox peaks can be noted on the CV at scan rates from 100 to 5 mVs^{-1} (Figure 7B, Figure S14). A decrease of the double-layer capacitance is observed and may be explained by the increase of the distance separating electrolyte ions from the electrode surface after enzyme adsorption.[40] Note also that the occurrence of background signals at negative potentials thought to originate from quinone and other groups at defect spots on CNT complicating the quantification of the non-catalytic signals (Figure 7).

Although the non-catalytic signal of the [NiFe] active centre of non-inhibited hydrogenase cannot be detected in the aqueous solutions because of the reversible proton reduction, the higher potential [FeS]-clusters are susceptible to be identified.[38] We thus attempted to attribute the redox peaks on the basis of EPR titrations previously performed for *Aa* MBH.[41] The peak at -0.29 V corresponds well to the midpoint potential of the distal [4Fe4S] cluster of *Aa* MBH, which is the last electron relay in the enzyme before the electrode (potential -0.275±0.02 V vs Ag/AgCl at pH 7.4). Concerning the peak at -0.07 V, which seems to be larger than the one-electron peak of the distal cluster, it might be a superposition of multiple peaks from the medial [3Fe4S] cluster (-0.129±0.02 V vs Ag/AgCl at pH 7.4) and the two redox states of the proximal [4Fe3S] cluster (-0.11±0.02 V and 0.035±0.02 V respectively vs Ag/AgCl at pH 7.4). The low potential peak at -0.45 V cannot be attributed to any [FeS] cluster observable by EPR but its potential is still too high to suggest one of the states of the [NiFe] active centre.

In order to attribute the observed peaks with certainty, the electrode was left in the open cell for several days. This induced a gradual denaturation of the enzyme, which was transduced into both catalytic (Figure S15A) and non-catalytic signals. Assuming that non-catalytic peaks were proportional to the quantity of active enzymes adsorbed, i.e. to the catalytic response, we studied the correlation of the integrative charges of the CV peaks at -0.45 V and -0.29 V with the catalytic

current at -0.4 V (the peak at -0.07 V was omitted as it was impossible to reliably subtract the baseline in that region) (Figure S15B, C). Both peaks heights were proportional to the scan rate in the 5 to 100 mV s^{-1} range, confirming that the redox moieties were effectively adsorbed on the electrode (Figure S14B). The peak at -0.45V displayed weak correlation with the catalytic current at all scan rates (Figure S15B) evoking the possibility that this redox transition was not related to *Aa* MBH. The origin of this signal is still under investigation, but it most probably arises from non-proteic redox contaminant present in the enzyme sample. On the other hand, the peak at -0.29 V demonstrated good correlations with the catalytic current (Pearson's correlation coefficient 0.998) (Figure 7C, Figure S15C). This corroborates the earlier attribution of this peak to the distal [4Fe4S] cluster of the adsorbed electroactive *Aa* MBH molecule, in full conformity with a role of this cluster as the last electronic relay communicating directly with the electrode.[29]

Non-catalytic signals for *Bp* BOD have already been reported and a redox peak at 0.55 V (pH 4) detected on carbon nanofibers has been attributed to the T1 copper centre.[42] In this work, two pairs of peaks appeared on SWV and CV in the 0.2-0.6 V potential range at scan rates from 2 to 100 mV s^{-1} (Figure 8, Figure S16A, B). The more intense, well-defined wave was centred around 0.47 V and would correspond to the T1 copper centre.[42] The potential of this peak changed with pH, with a slope of 45 mV (Figure 8B, Figure S16C).The second, smaller, broad peak centred around 0.35 V might be attributed to the molecules orientated with the T2/T3 copper centre towards the electrode, as recently proposed for laccase and *Myrothecium verrucaria Bp* BOD.[43–45] However, it seemed too wide for the 3-electron transfer process expected for this centre, and had an unexpected pH-dependence slope of 20 mV (Figure S16C). We thus assume hereafter that bioelectrocatalysis occurs through DET of *Bp* BOD molecules facing the electrode surface by the T1 copper centre presenting a redox potential of 0.47 V.

Determination of the electroactive fraction of enzymes.

Based on the distal cluster peak at -0.29 V, the electroactive amount of *Aa* MBH adsorbed on the electrode was determined, considering a one-electron transfer for the $[4Fe4S]^{2+/1+}$ cluster. The integration of this reductive peak at different scan rates gave a total of 0.17±0.03 nmol of electroactive *Aa* MBH on the electrode from the 1.43 nmol added into the cell. At the same time, the UV-Vis measurement of remaining *Aa* MBH activity in the cell after adsorption showed that 0.22±0.09 nmol of enzyme remained unadsorbed in the solution. Thus, only 14% of *Aa* MBH adsorbed on the electrode was electroactive. Taking this amount into account, the true turnover constant of *Aa* MBH for hydrogen oxidation at 25 °C was found to be 94 (SD 7) s^{-1} and 155 (SD

11) s^{-1} at -0.3 V and 0 V respectively, *i.e.* very close to the value of about 100 s^{-1} obtained for the homologous hydrogenase from *Ralstonia eutropha* in a solution-based assay in similar conditions.[6]

The integration of the anodic cyclic voltammetry peak at 0.47 V allowed the amount of electroactive *Bp* BOD adsorbed on the CF-CNT to be determined, assuming one T1 copper centre per molecule exchanging one electron.[37] The same quantity of electroactive *Bp* BOD 0.34±0.01 nmol was found by integration of non-catalytic signals at scan rates from 2 to 20 mV s^{-1} (Figure S16D). Considering the total quantities of 4.12 nmol added and 0.17±0.02 nmol found in the cell after adsorption equilibrium had become established, the amount of electroactive *Bp* BOD made up only approximately 9 % of the total quantity of adsorbed *Bp* BOD. The new turnover constant at 25 °C determined with the electroactive quantity was then found to be 40±1 s^{-1} at 0.3 V and 102±3 s^{-1} at 0 V, which is very close to the values in the solution-based assay with ABTS and again confirms the accuracy of the analysis.

For both enzymes, although the enzymes participating in the current were very efficient, 90% of the total enzyme amount incorporated in the porous matrix was not electroactive. One explanation could be a rapid deactivation or denaturation of the enzymes upon contact with the surface. However, electrochemical measurements have revealed high stability of the catalytic current, making this hypothesis unlikely. A more plausible explanation for the low ratio of electroactive enzymes would be the absence of electrical connection between most of the enzyme molecules and the electrode. As shown also in our previous work on CNT thin films,[16] the addition of a mediator in the case of *Bp* BOD gives rise to a mediated current. The ratio of mediated to direct catalytic current obtained after the mediator addition was *ca.* 8, i.e. very close to the value expected in the case of the poor connection of 90 % of enzyme molecules, thus confirming our conclusions (Figure S17). This also suggests that despite the net improvement induced by the $PyrNH_2$ surface modification, there is room for enhancing the amount of molecules oriented for DET by enzyme engineering or more specific surface functionalization.

Knowing the initial amount of catalyst and the deactivation rate constant previously defined in the stability experiments, it is possible to deduce the total turnover number (i.e. the turnover number achieved before full degradation of the catalyst) for both enzymes (Figure S11). It reaches high values of 10^7-10^6 for *Bp* BOD, depending on whether electroactive or total enzyme coverage is taken for the calculation (See explanation in the SI). At the same time, the total turnover number of *Aa* MBH was found to be more than one order of magnitude higher, i.e. 6×10^8-10^8, depending on whether electroactive or total enzyme coverage was taken for the calculation. To the best of our knowledge, this is the first time the total turnover number has been calculated for immobilized

redox enzymes. Their very high values highlight the advanced combination of high activity and stability of the biocatalysts used in this work.

Furthermore, the knowledge of the real amount of electroactive enzyme leads to an important conclusion concerning bioelectrocatalysis (Table 4). If the total enzyme loading is taken into account, catalyst-specific current densities from 47 (25 °C) to 151 (50 °C) mA mg^{-1} with *Aa* MBH and from 44 (25 °C) to 76 (50 °C) mA mg^{-1} with *Bp* BOD can be calculated. To the best of our knowledge these values surpass the catalyst-specific current densities of all the bioelectrodes used in EFC developed within the past two years (Table 2). Moreover, these values are enhanced by one order of magnitude if the amount of electroactive catalyst as determined from non-catalytic signals is taken into consideration. In this case, outstanding current density values of up to 1 A mg^{-1} at 50 °C can be obtained for both enzymes (Table 4).

Conclusions

The present work has demonstrated an advanced benchmark H_2/O_2 EFC, based on the combination of two thermostable enzymes and their direct efficient wiring in porous material with suitable chemical functionalization. A mesoporous network with pore size in the range 10 – 40 nm was created by layer-by-layer deposition of CNTs on macroporous carbon fibres, favouring both *Aa* MBH and *Bp* BOD adsorption even from dilute solutions. An in-depth analysis of the adsorption process determined thermodynamic adsorption constants in the order of 10^8 M^{-1}, indicating strong physisorption of both enzymes on the CNT-based materials. One original result of this work was the detection of non-catalytic signals for *Bp* BOD and, even more interestingly, for *Aa* MBH thanks to the increase in enzyme loading in the porous material. Actually, this type of signal was lacking for most hydrogenases and many other redox enzymes, thus essential kinetics data were unknown. The quantity of electroactive enzyme molecules truly participating in the electrocatalysis could thus be calculated. In both cases, it was shown that 10-15 % of the total quantity of adsorbed enzymes contributed to the bioelectrocatalysis. As suggested by the analysis of the mediated current, increase in this percentage most probably implies enzyme engineering and/or new functionalization of mesoporous materials, despite great improvement already achieved here thanks to nanotube chemical modification. This corresponded to very high catalyst-specific current densities of 335 mA mg^{-1} for H_2 oxidation by *Aa* MBH, and 488 mA mg^{-1} for O_2 reduction by *Bp* BOD at 25 °C, which increased to 1.08 and 0.84 A mg^{-1} respectively at 50 °C thanks to the thermostability of both enzymes. It should be noted that the Fuel Cell Technologies Office of the U.S. Department of Energy has set the target of mass activity of 0.44 A mg^{-1} at 0.9 V

and 80 °C for platinum group metals by 2020.[46] Although measured at another potential, enzymatic mass-specific current densities obtained in this work come close to this target. Our results thus clearly highlight the great potentialities of thermostable and more generally extremophilic enzymes for bioelectrocatalysis. The incorporation of the enzymes into a suitable porous matrix also appears to be advantageous in terms of bioelectrode stability, providing long-term stability and total turnover numbers in the order of 10^7-10^8. Such porous matrix offers also perspectives in the protection of enzymatic and molecular catalysts against the ROS inevitably formed on the electrodes in the presence of oxygen at low potentials. One relevant example is artificial photosynthesis and water splitting by enzymes or molecular catalysts that must be protected against O_2 and ROS.[33]

3D porous materials thus appear to be a good choice in terms of biocatalyst electrical wiring and stability. However, incorporating high amounts of catalysts into such materials induces fast substrate depletion, especially with highly-active enzymes such as hydrogenases and multicopper oxidases. In this work, the mass transfer was fully analysed by electrochemistry and by modelling. An optimal electrode thickness less than 100 μm was thus determined. This numerical modelling allowed the best geometry to be defined for the EFC, and maximum current and power densities of 1.3 mA cm^{-2} and 0.5 mW cm^{-2}, respectively, at 25 °C to be anticipated in quiescent conditions. These performances can be significantly enhanced if the substrate supply is enhanced by artificial convection. The design of such systems using microfluidic devices, low-power pumps or rotating electrodes, and the estimation of the associated power loss would be an interesting future topic. Furthermore, the abundant hydrogen conditions provided by these systems can decrease the technologically relevant apparent rate of anaerobic hydrogenase deactivation. Beyond this current study, the FEM numerical model that has been set up in this work will certainly be useful for investigating other parameters affecting EFC operation and, more generally, electrodes based on enzyme immobilization. It can be anticipated that substrate diffusion limitation found in this work will occur in other bioelectrodes based on the enzymes whose substrate is a gas at normal conditions. Besides hydrogenases and multicopper oxidases, one can cite carbon monoxide dehydrogenases[47] or nitrogenases[48,49] which are technologically relevant within a friendly environmental context.

Acknowledgements

This work was supported by A*MIDEX Marseille (ANR-11-IDEX-0001-02) and by ANR (CAROUCELL-ANR-13-BIOME-0003-02). The authors thank Dr R. Denoyel (MADIREL,

Marseille) for the porosity measurements. This work benefited from the facilities and expertise of the Platform for Microscopy of IMM. The authors would also like to thank Dr A. de Poulpiquet (BIP, Marseille) for fruitful discussion.

References

1 K. Ma and N. Ibrahim, *Curr. Biochem. Eng.*, 2017, **04**, in press.

2 I. Mazurenko, X. Wang, A. de Poulpiquet and E. Lojou, *Sustain. Energy Fuels*, 2017, in press.

3 K. Monsalve, I. Mazurenko, N. Lalaoui, A. Le Goff, M. Holzinger, P. Infossi, S. Nitsche, J. Y. Lojou, M. T. Giudici-Orticoni, S. Cosnier and E. Lojou, *Electrochem. Commun.*, 2015, **60**, 216–220.

4 L. Xu and F. A. Armstrong, *RSC Adv.*, 2015, **5**, 3649–3656.

5 A. F. Wait, A. Parkin, G. M. Morley, L. Dos Santos and F. A. Armstrong, *J. Phys. Chem. C*, 2010, **114**, 12003–12009.

6 M. Ludwig, J. A. Cracknell, K. A. Vincent, F. A. Armstrong and O. Lenz, *J. Biol. Chem.*, 2009, **284**, 465–477.

7 M. E. Pandelia, V. Fourmond, P. Tron-Infossi, E. Lojou, P. Bertrand, C. Léger, M. T. Giudici-Orticoni and W. Lubitz, *J. Am. Chem. Soc.*, 2010, **132**, 6991–7004.

8 N. Plumeré, O. Rüdiger, A. A. Oughli, R. Williams, J. Vivekananthan, S. Pöller, W. Schuhmann and W. Lubitz, *Nat. Chem.*, 2014, **6**, 822–7.

9 P. O Conghaile, M. Falk, D. MacAodha, M. E. Yakovleva, C. Gonaus, C. K. Peterbauer, L. Gorton, S. Shleev and D. Leech, *Anal. Chem.*, 2016, **88**, 2156–2163.

10 A. A. Oughli, F. Conzuelo, M. Winkler, T. Happe, W. Lubitz, W. Schuhmann, O. Rüdiger and N. Plumeré, *Angew. Chem., Int. Ed.*, 2015, **54**, 12329–12333.

11 V. Fourmond, S. Stapf, H. Li, D. Buesen, J. Birrell, O. Rüdiger, W. Lubitz, W. Schuhmann, N. Plumeré and C. Léger, *J. Am. Chem. Soc.*, 2015, **137**, 5494–5505.

12 K. So, Y. Kitazumi, O. Shirai, K. Nishikawa, Y. Higuchi and K. Kano, *J. Mater. Chem. A*, 2016, **4**, 8742–8749.

13 H. qi Xia, K. So, Y. Kitazumi, O. Shirai, K. Nishikawa, Y. Higuchi and K. Kano, *J. Power Sources*, 2016, **335**, 105–112.

14 A. de Poulpiquet, A. Ciaccafava, R. Gadiou, S. Gounel, M. T. Giudici-Orticoni, N. Mano and E. Lojou, *Electrochem. Commun.*, 2014, **42**, 72–74.

15 A. Ciaccafava, P. Infossi, M. Ilbert, M. Guiral, S. Lecomte, M. T. Giudici-Orticoni and E. Lojou, *Angew. Chem. Int. Ed. Engl.*, 2012, **51**, 953–6.

16 I. Mazurenko, K. Monsalve, J. Rouhana, P. Parent, C. Laffon, A. Le Goff, S. Szunerits, R. Boukherroub, M.-T. Giudici-Orticoni, N. Mano and E. Lojou, *ACS Appl. Mater. Interfaces*, 2016, **8**, 23074–23085.

17 K. Monsalve, I. Mazurenko, C. Gutierrez-Sanchez, M. Ilbert, P. Infossi, S. Frielingsdorf, M. T. Giudici-Orticoni, O. Lenz and E. Lojou, *ChemElectroChem*, 2016, **3**, 2179–2188.

18 P. Rodriguez-Maciá, A. Dutta, W. Lubitz, W. J. Shaw and O. Rüdiger, *Angew. Chem., Int. Ed.*, 2015, **54**, 12303–12307.

19 L. Rajendran, M. Kirthiga and E. Laborda, *Curr. Opin. Electrochem.*, 2017, **1**, 121–132.

20 M. Brugna-Guiral, P. Tron, W. Nitschke, K. O. Stetter, B. Burlat, B. Guigliarelli, M. Bruschi and M.-T. Giudici-Orticoni, *Extremophiles*, 2003, **7**, 145–157.

21 S. Gounel, J. Rouhana, C. Stines-Chaumeil, M. Cadet and N. Mano, *J. Biotechnol.*, 2016, **230**, 19–25.

22 J. P. McGann, M. Zhong, E. K. Kim, S. Natesakhawat, M. Jaroniec, J. F. Whitacre, K. Matyjaszewski and T. Kowalewski, *Macromol. Chem. Phys.*, 2012, **213**, 1078–1090.

23 E. P. Barrett, L. G. Joyner and P. P. Halenda, *J. Am. Chem. Soc.*, 1951, **73**, 373–380.

24 E. W. Washburn, *Phys. Rev.*, 1921, **17**, 273–283.

25 Y. Sugimoto, Y. Kitazumi, O. Shirai and K. Kano, *Electrochemistry*, 2017, **85**, 82–87.

26 E. Suraniti, S. Tsujimura, F. Durand and N. Mano, *Electrochem. Commun.*, 2013, **26**, 41–44.

27 R. T. Bonnecaze, N. Mano, B. Nam and A. Heller, *J. Electrochem. Soc.*, 2007, **154**, F44.

28 V. Flexer, N. Brun, O. Courjean, R. Backov and N. Mano, *Energy Environ. Sci.*, 2011, **4**, 2097–2106.

29 K. A. Vincent, A. Parkin and F. A. Armstrong, *Chem. Rev.*, 2007, **107**, 4366–4413.

30 J. Fischer, R. Ulbrich, R. Ziemann, S. Flatau, P. Wolna, M. Schleiff, V. Pluschke and A. Schellenberger, *J. Solid-Phase Biochem.*, 1980, **5**, 79–96.

31 S. Lebedkin, I. Kareev, F. Hennrich and M. M. Kappes, *J. Phys. Chem. C*, 2008, **112**, 16236–16239.

32 P. Boldog, K. Hajdu, M. Magyar, E. Hideg, K. Hernadi, E. Horvath, A. Magrez, K. Nagy, G. Varo, L. Forro and L. Nagy, *Phys. Status Solidi Basic Res.*, 2013, **250**, 2539–2543.

33 D. W. Wakerley and E. Reisner, *Energy Environ. Sci.*, 2015, **8**, 2283–2295.

34 L. Xu and F. A. Armstrong, *Energy Environ. Sci.*, 2013, **6**, 2166–2171.

35 D. Ivnitski, K. Artyushkova and P. Atanassov, *Bioelectrochemistry*, 2008, **74**, 101–110.

36 N. Lalaoui, A. Le Goff, M. Holzinger and S. Cosnier, *Chem. - Eur. J.*, 2015, **21**, 16868–16873.

37 P. Ramírez, N. Mano, R. Andreu, T. Ruzgas, A. Heller, L. Gorton and S. Shleev, *Biochim. Biophys. Acta - Bioenerg.*, 2008, **1777**, 1364–1369.

38 H. R. Pershad, J. L. C. Duff, H. A. Heering, E. C. Duin, S. P. J. Albracht and F. A. Armstrong, *Biochemistry*, 1999, **38**, 8992–8999.

39 A. Parkin, G. Goldet, C. Cavazza, J. C. Fontecilla-Camps and F. A. Armstrong, *J. Am. Chem. Soc.*, 2008, **130**, 13410–13416.

40 A. J. Bard and L. R. Faulkner, *Electrochemical methods: fundamentals and applications*, John Wiley & Sons, 2nd edn., 2001.

41 M.-E. Pandelia, W. Nitschke, P. Infossi, M.-T. Giudici-Orticoni, E. Bill and W. Lubitz, *Proc. Natl. Acad. Sci. U. S. A.*, 2011, **108**, 6097–6102.

42 A. de Poulpiquet, C. H. Kjaergaard, J. Rouhana, I. Mazurenko, P. Infossi, S. Gounel, R. Gadiou, M. T. Giudici-Orticoni, E. I. Solomon, N. Mano and E. Lojou, *ACS Catal.*, 2017, **7**, 3916–3923.

43 S. Shleev, V. Andoralov, M. Falk, C. T. Reimann, T. Ruzgas, M. Srnec, U. Ryde and L. Rulíšek, *Electroanalysis*, 2012, **24**, 1524–1540.

44 N. Lalaoui, M. Holzinger, A. Le Goff and S. Cosnier, *Chem. - Eur. J.*, 2016, **22**, 10494–10500.

45 M. Dagys, A. Laurynėnas, D. Ratautas, J. Kulys, R. Vidžiūnaitė, M. Talaikis, G. Niaura, L. Marcinkevičienė, R. Meškys and S. Shleev, *Energy Environ. Sci.*, 2017, **10**, 498–502.

46 F. C. T. (FCT) Office and U. S. D. of E. (DOE's) O. of E. E. and R. E. (EERE), *Fuel Cell Technologies Office Multi-Year Research, Development, and Demonstration (MYRD&D) Plan*, 2016, vol. 3.4.

47 M. Merrouch, J. Hadj-Saïd, L. Domnik, H. Dobbek, C. Léger, S. Dementin and V. Fourmond, *Chem. - Eur. J.*, 2015, **21**, 18934–18938.

48 R. D. Milton, S. Abdellaoui, N. Khadka, D. R. Dean, D. Leech, L. C. Seefeldt and S. D. Minteer, *Energy Environ. Sci.*, 2016, **9**, 2550–2554.

49 R. D. Milton, R. Cai, S. Abdellaoui, D. Leech, A. L. De Lacey, M. Pita and S. D. Minteer, *Angew. Chem., Int. Ed.*, 2017, **56**, 2680–2683.

50 K. Monsalve, M. Roger, C. Gutiérrez-Sánchez, M. Ilbert, S. Nitsche, D. Byrne-Kodjabachian, V. Marchi and E. Lojou, *Bioelectrochemistry*, 2015, **106**, 47–55.

51 N. Lalaoui, A. de Poulpiquet, R. Haddad, A. Le Goff, M. Holzinger, S. Gounel, M. Mermoux, P. Infossi, N. Mano, E. Lojou and S. Cosnier, *Chem. Commun.*, 2015, **51**, 7447–7450.

Figure captions:

Figure 1. (A) SEM images with magnification 20000x of CF-fibre (left) before and (right) after modification with CNTs; (B) Nitrogen adsorption/desorption isotherms of (black) CF and (red) CF-CNT. Inset: Distribution of pore sizes for CF-CNT calculated by BJH-model from the high pressure region of the N_2 isotherm desorption branch.

Figure 2. (A) Separate CVs at different temperatures of (red lines) bioanode and (blue lines) biocathode in the EFC-configuration. Phosphate buffer pH 6, 0.2 M, 1000 rpm, scan rate 5 mV s^{-1}, 100% H_2 or 100 % O_2; (B) Polarization curves of the EFC at different temperatures in the galvanostatic mode. Step increments of 0.25 mA were applied for 60 s; phosphate buffer pH 6, 0.2 M, 1000 rpm, 100% H_2 or 100 % O_2. (C) Stability experiment with the EFC in the galvanostatic mode at 25 °C and 1.5 mA. The curves correspond to (black lines) EFC voltage, (red lines) bioanode potential, (blue lines) biocathode potential and (green lines) power produced. Phosphate buffer pH 6 0.2 M, 1000 rpm, 100% H_2 or 100 % O_2; (D) Polarization curves of the EFC at (filled symbols) 25 °C and (empty symbols) 40 °C in the galvanostatic mode in the absence of forced convection. Step increments of 0.025 mA were applied for 60 s, phosphate buffer pH 6, 0.2 M, 0 rpm, 100% H_2 or 100 % O_2 atmosphere above the solution. The cylindrical electrodes external surface area was 1.34 cm^2 in all cases.

Figure 3. (A) 3D representation of the single compartment of the EFC used for the modelling and simulation of the catalytic curves in stationary conditions. Colour scale shows an example of substrate concentration distribution: H_2 concentration after one CV scan from -0.6 V to 0 V at 5 mV s^{-1}; (B, C) CVs at (black lines) 4000 rpm (only forward half-cycle) and (red lines) 0 rpm of the (B) bioanode and (C) biocathode. Blue dashed lines show simulated voltammograms at 0 rpm (stationary conditions). Phosphate buffer pH 6 0.2 M, 25 °C, scan rate 5 mV s^{-1}, 100% H_2 or 100 % O_2; (D, E) Profile of corresponding substrate concentration for (D) bioanode and (E) biocathode in stationary conditions as a function of both applied potential (assuming potential scan at 5 mV s^{-1}) and the distance from the bioelectrode centre (along yellow dashed line on (A)).

Figure 4. Representation of the 2D-model used for the study of the optimal EFC configuration. Colour gradients show an arbitrary example of substrate concentration expected within the EFC; (B, C) Simulated geometric maximum current and power densities of the H_2-air EFC as a function of (B) bioelectrode thickness or (C) bioelectrode compression factor.

Figure 5. O_2-resistance chronoamperometry experiments of *Aa* MBH: (A) CF-CNT-*Aa* MBH was subjected to a constant potential of -0.4 V and the cell atmosphere was changed according to the sequence at the top of the graph. In all cases, the N_2 "buffer" was intercalated in

order to prevent direct contact of H_2 and O_2, and so the establishment of a mixed potential. The circuit was disconnected during the oxygen bubbling in the first two cases and the OCP of the electrode was followed (right axis). Phosphate buffer pH 7 0.2 M, 25 °C, 1000 rpm. (B) Normalized chronoamperometric curves of (black line) 3D CF-CNT-*Aa* MBH and (red line) 2D PG-CNT-*Aa* MBH at a constant potential of -0.4 V and 1000 rpm. The cell atmosphere was switched from 100% H_2 to 93% H_2 - 7% O_2 as indicated at the top of the graph. Phosphate buffer pH 7 0.2 M, 25 °C. A unit of normalized current corresponds to (black line) 1.45 mA and (red line) 23.5 μA.

Figure 6. (A, B) Equilibrium CVs of CF-CNT after addition of indicated amounts of (A) *Bp* BOD (pH 6) or (B) *Aa* MBH (pH 7). Cell volume 10 mL, phosphate buffer 0.2 M, 1000 rpm, 25 °C, scan rate 5 mV s^{-1}, (A) 100 % O_2 or (B) 100% H_2 atmosphere; (C, D) Adsorption isotherms of (C) *Bp* BOD and (D) *Aa* MBH, solid lines show the fit of experimental points to the Langmuir equation. Current densities are normalized to the electrode electroactive surface area.

Figure 7. (A) Consecutive SVWs of CF-CNT (black line) before and (coloured lines) after addition of 1.43 nmol of *Aa* MBH. Inset demonstrates the same voltammograms after blank subtraction. Phosphate buffer pH 7 0.2 M, 1000 rpm, 25 °C, SWV frequency 1 Hz, amplitude 20 mV, step 2 mV; (B) CVs of CF-CNT under N_2 atmosphere (black line) before and (red line) after adsorption of *Aa* MBH (1.43 nmol added to the cell). Phosphate buffer pH 7 0.2 M, 0 rpm, scan rate 50 mV s^{-1}, 25 °C; Inset: Zoom of the anodic and cathodic branches of the CF-CNT-*Aa* MBH; (C) Correlation of the catalytic current at -0.4 V with the charge obtained from the integration of the cathodic peak at -0.29 V at different scan rates. Inset: corresponding turnover constants of *Aa* MBH at different potentials.

Figure 8. (A) CVs of CF-CNT at different scan rates under N_2 atmosphere (black lines) before and (red lines) after adsorption of *Bp* BOD (4.12 nmol added to the cell). Phosphate buffer pH 6 0.2 M, 0 rpm, 25 °C; Inset: Zoom of the anodic and cathodic branches of the CF-CNT-*Bp* BOD; (B) SWVs of CF-CNT-*Bp* BOD under N_2 atmosphere at different pH. Dashed line shows the blank CF-CNT at pH 6. Phosphate buffer 0.2 M, 0 rpm, 25 °C, SWV frequency 0.5 Hz, amplitude 20 mV, step 2 mV.

Table 1. Summary of bioelectrode and EFC characteristics at different temperatures. All values were measured and calculated assuming the absence of mass-transfer limitations.

	Absolute			**Specific (Surface)**			**Specific (Volumetric)**		
	Current at 0 V, mA		Maximum power, mW	Current density at 0 V, mA cm^{-2}		Maximum power density, mW cm^{-2}	Current density at 0 V mA cm^{-3}		Maximum volumetric power density, mW cm^{-3}
	Anode	Cathode		Anode	Cathode		Anode	Cathode	
25 °C	6.5	15.8	1.3	4.9	11.8	1.0	55	134	40
30 °C	8.3	19.2	1.5	6.2	14.4	1.1	70	163	55
40 °C	14.3	23.5	1.9	10.7	17.6	1.4	121	199	70
50 °C	20.9	27.2	2.3	15.7	20.3	1.7	178	231	85

Table 2. Some characteristics of the H_2/O_2 EFCs developed during the past two years. (A refers to anode or to anode area/loading; C refers to cathode or to cathode area/loading; FC refers to fuel cell)

Year	Bioanode	Biocathode	Substrates	Membrane	T, °C	Max absolute power, mW	Max power density, mW/cm^2	Max geometric current densities, mA/cm^2	Max catalyst specific current densities, mA/mg	Stability	Specific conditions	Ref.
2015	*Aa* MbH	*Mv* BOD	(A): H_2 (C): O_2	yes	(A): 60 (C): 25		0.25	(A)1.6 (FC): 0.65		n.d.	Gas bubbling	[50]
2015	*Cr* HydA1 [FeFe]-Hase in MeV-based hydrogels	*Mv* BOD	95% H_2 - 5% O_2	no	25	0.016	(A): 0.225 (C): 0.001	(A) 0.44 (FC): 0.25	(A)0.86 (FC): 0.26	18 h	Cathode / anode surface area = 200	[10]
2015	*E. coli* Hyd1	*Mv* BOD	78% H_2 - 22% O_2	no	20	0.61 (1x1 cell) 8 (2x(4x4))	(A):0.5 (C):0.1	(A) 1.5 (C) 0.46	(A) 15 (C) 3	No decrease in the intensity of a powered LED for 8 h	Cathode / anode surface area = 5 Gas bubbling	[4]
2015	*Aa* MbH	*Mv* BOD	(A): H_2 (C): O_2	yes	(A): 60 (C): 25	0.41	0.28	(A) 1.2 mA (C) 1.4 mA	(A) 18 (C) 11	Data sent wirelessly every 25 s during 7 h	Gas bubbling	[3]
2015	*Aa* MbH	*Bp* BOD	(A): H_2 (C): air	no	45	0.05	0.72	(A) 1.4 (C) 3	(A) 9 (C) 35	Visible loss within 1000 s	(A): H_2 bubbling (C): Air-breathing,	[51]
2016	*Dv* Miyazaki MbH	*Mv* BOD	(A): H_2 (C): air	no	25	6.1	6.1	(C) 11.2 (A) 15.8	(A) 32 (C) 1.9	Visible loss within 60 s	Gas diffusion system	[13]
2016	*Dv* Miyazaki MbH	*Mv* BOD	(A): H_2 (C): O_2	no	40	8	8.4 (calculated from the half cells)	(C) 20 (A) 10	(A) 9.3 (C) 4.7	Visible loss within 60 s	Gas diffusion system	[12]
2017	***Aa* MBH**	***Bp* BOD**	**(A): H_2 (C): O_2**	**yes**	**25**	**1.3**	**1**	**(A) 4.9 (C) 11.8**	**(A) 47 (El-active: 335) (C) 44 (El-active: 488)**	**5% loss after 17 h at 25 C**	**Rotating electrode**	**This work**
					50	**2.3**	**1.7**	**(A) 15.7 (C) 20.3**	**(A) 151 (El-active: 1077) (C) 76 (El-active: 839)**	**n.d.**		
			(A): H_2 (C): air (modelled)	**no**	**25**	-	**0.5**	**(FC): 1.3**		-	**Stationary electrode (modelled)**	

Table 3. Summary of Langmuir equation parameters obtained from the fit of adsorption data for *Bp* BOD and *Aa* MBH.

	Langmuir isotherm (quantity)			**Apparent turnover rate (O_2 or H_2)**	
	Γ_{max}, pmol cm^{-2}	$K_L \times 10^{-8}$, M^{-1}	R^2	k at ±0.3V, s^{-1}	k at 0V, s^{-1}
***Bp* BOD**	12.5±0.9	2.3±0.6	0.98	1.4±0.6 (SD)	4±2 (SD)
***Aa* MBH**	2.7±0.2	1.6±0.5	0.98	14±1 (SD)	23±2 (SD)

Table 4. Summary of bioelectrode and EFC characteristics normalized to catalyst loading. All values are calculated assuming the absence of mass-transfer limitations and a total quantity of adsorbed catalysts of 1.25 nmol (0.14 mg) of *Aa* MBH and 5.8 nmol (0.36 mg) of *Bp* BOD.

	Specific (Total Catalyst)			**Specific (Active Catalyst)**		
	Current density at 0V, mA mg^{-1}		Maximum power density, mW mg^{-1}	Current density at 0V, mA mg^{-1}		Maximum power density, mW mg^{-1}
	Anode	Cathode		Anode	Cathode	
25 °C	47	44	2.6	335	488	25.1
30 °C	60	53	3.0	425	592	28.9
40 °C	103	65	3.9	734	726	37.1
50 °C	151	76	4.7	1077	839	45.1

Figure 1

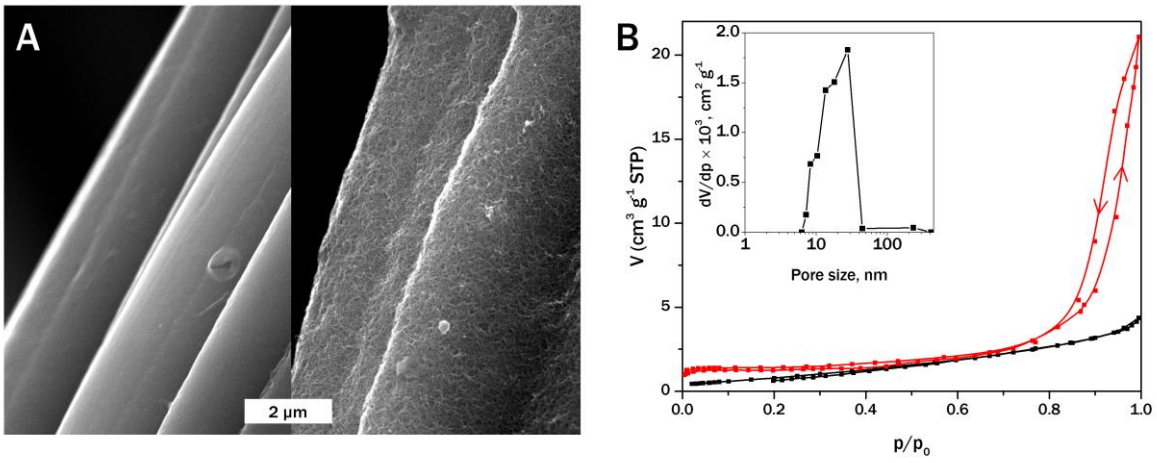

Figure 2

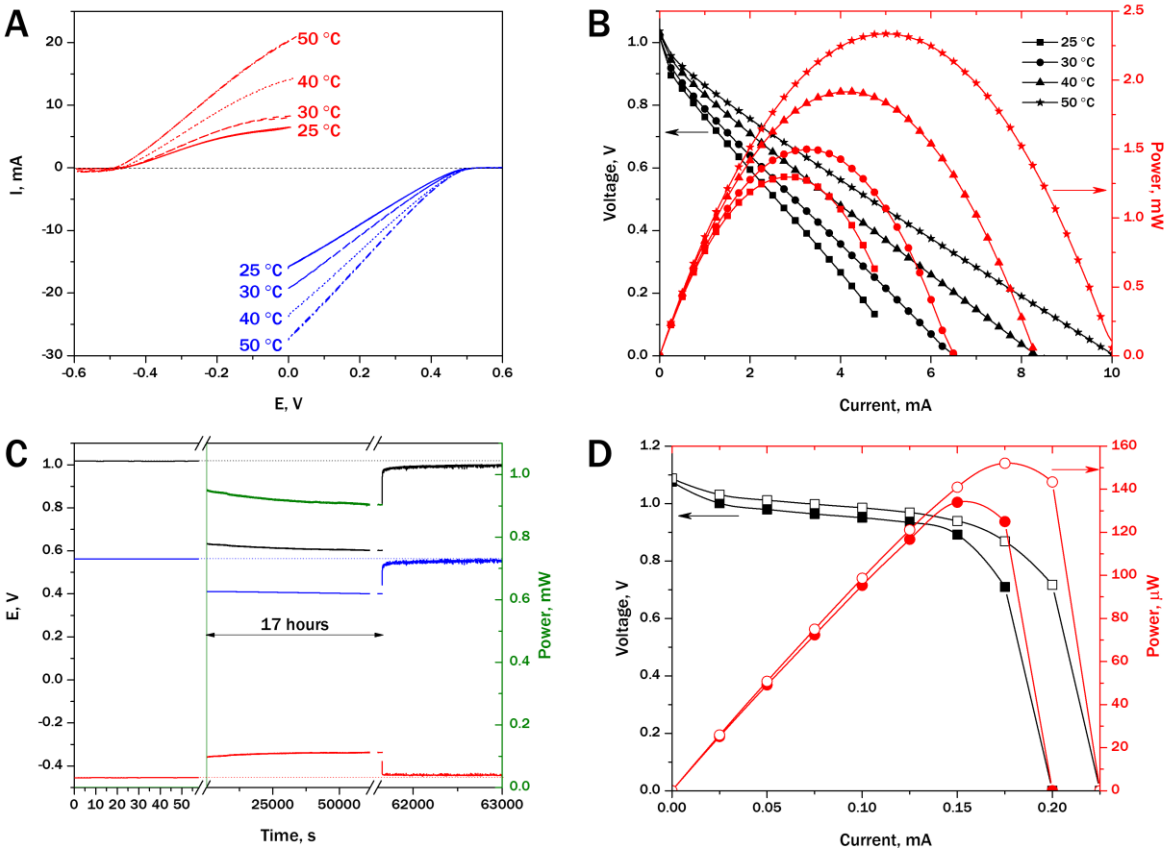
A
50 °C
40 °C
30 °C
25 °C
25 °C
30 °C
40 °C
50 °C
I, mA
E, V
B
25 °C
30 °C
40 °C
50 °C
Voltage, V
Power, mW
Current, mA
C
17 hours
E, V
Power, mW
Time, s
D
Voltage, V
Power, µW
Current, mA

Figure 3

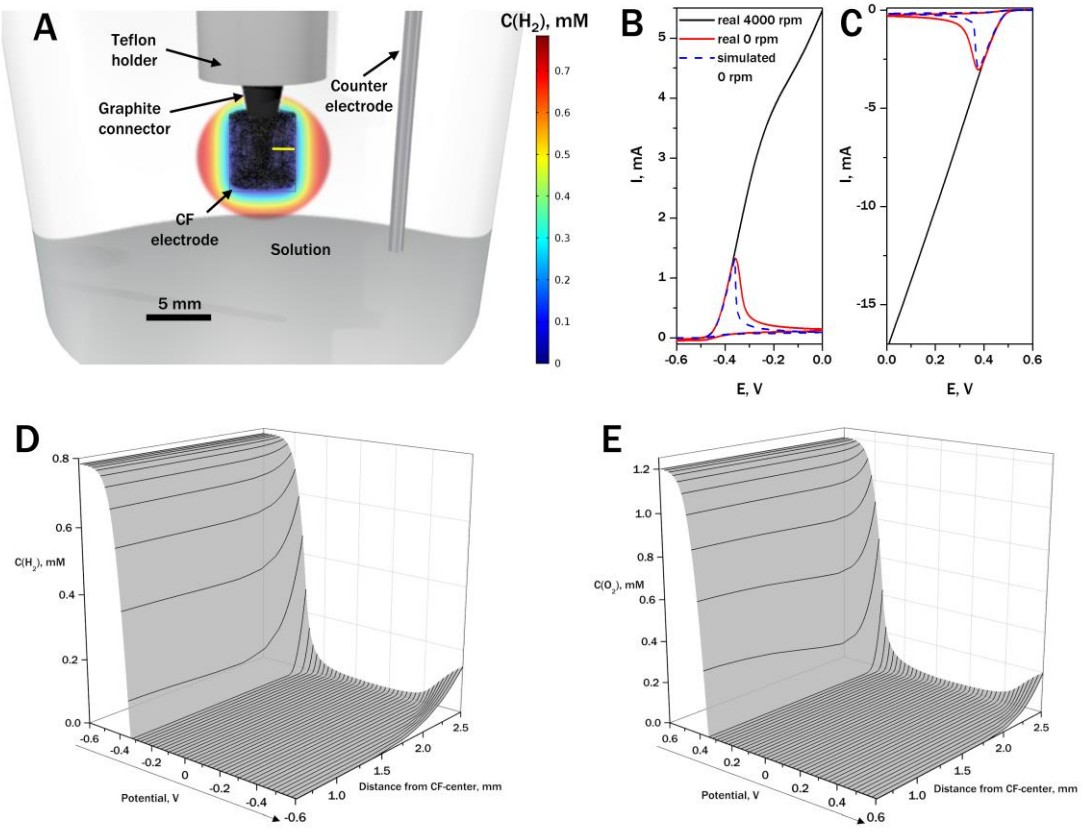
A
Teflon holder
Graphite connector
Counter electrode
CF electrode
Solution
5 mm
C(H2), mM
B
real 4000 rpm
real 0 rpm
simulated 0 rpm
I, mA
E, V
C
I, mA
E, V
D
C(H2), mM
Potential, V
Distance from CF-center, mm
E
C(O2), mM
Potential, V
Distance from CF-center, mm

Figure 4

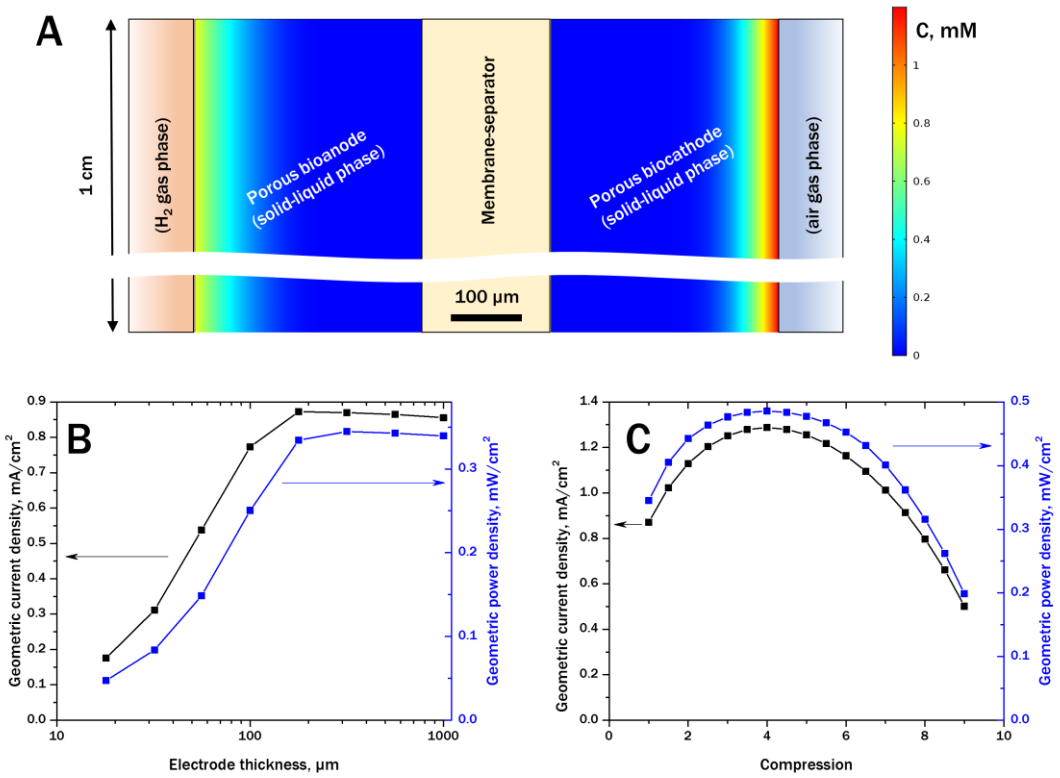
A
1 cm
(H2 gas phase)
Porous bioanode (solid-liquid phase)
Membrane-separator
Porous biocathode (solid-liquid phase)
(air gas phase)
100 µm
C, mM
1
0.8
0.6
0.4
0.2
0
B
Geometric current density, mA/cm2
Geometric power density, mW/cm2
Electrode thickness, µm
C
Geometric current density, mA/cm2
Geometric power density, mW/cm2
Compression

Figure 5

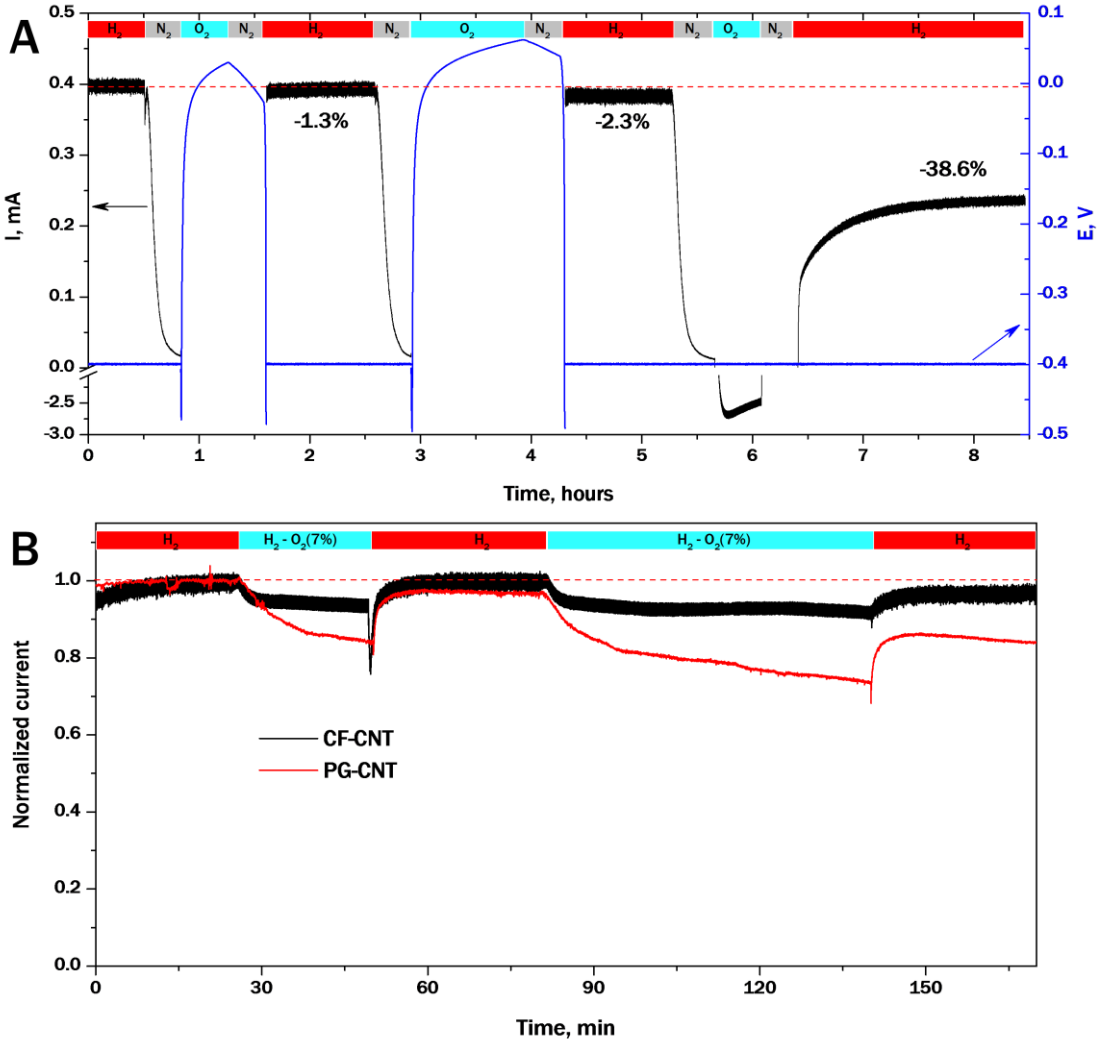
A
H2
N2
O2
N2
H2
N2
O2
N2
H2
N2
O2
N2
H2
-1.3%
-2.3%
-38.6%
I, mA
E, V
Time, hours
B
H2
H2 - O2(7%)
H2
H2 - O2(7%)
H2
Normalized current
CF-CNT
PG-CNT
Time, min

Figure 6

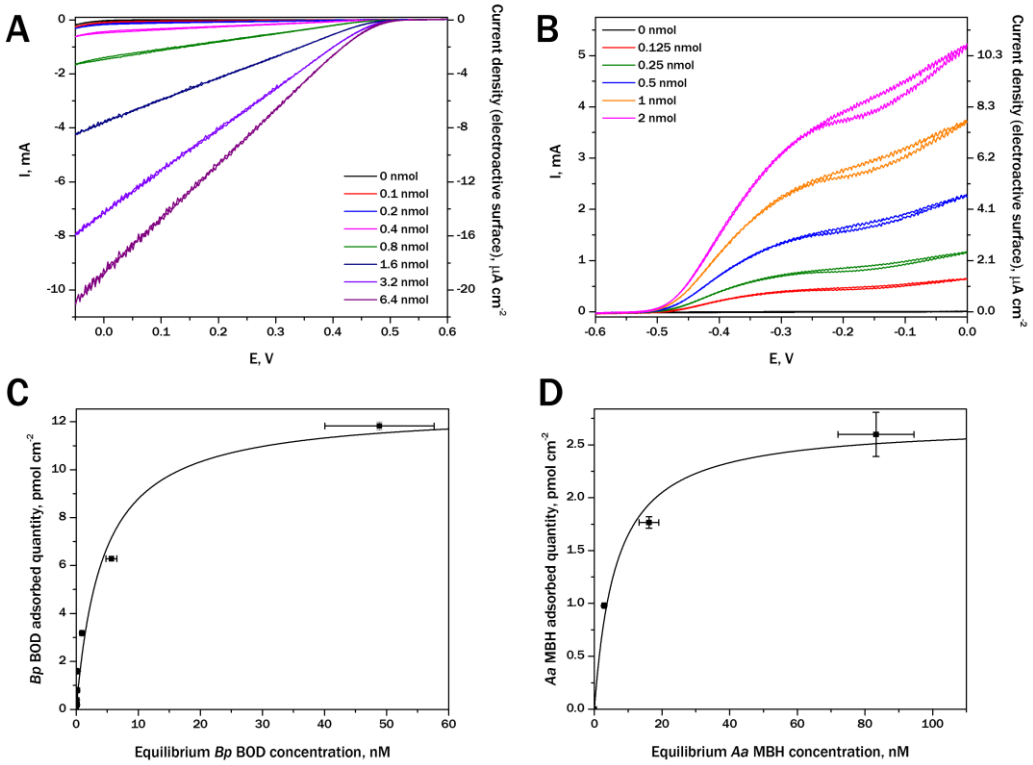
A
I, mA
Current density (electroactive surface), µA cm-2
E, V
0 nmol
0.1 nmol
0.2 nmol
0.4 nmol
0.8 nmol
1.6 nmol
3.2 nmol
6.4 nmol
B
I, mA
Current density (electroactive surface), µA cm-2
E, V
0 nmol
0.125 nmol
0.25 nmol
0.5 nmol
1 nmol
2 nmol
C
Bp BOD adsorbed quantity, pmol cm-2
Equilibrium Bp BOD concentration, nM
D
Aa MBH adsorbed quantity, pmol cm-2
Equilibrium Aa MBH concentration, nM

Figure 7

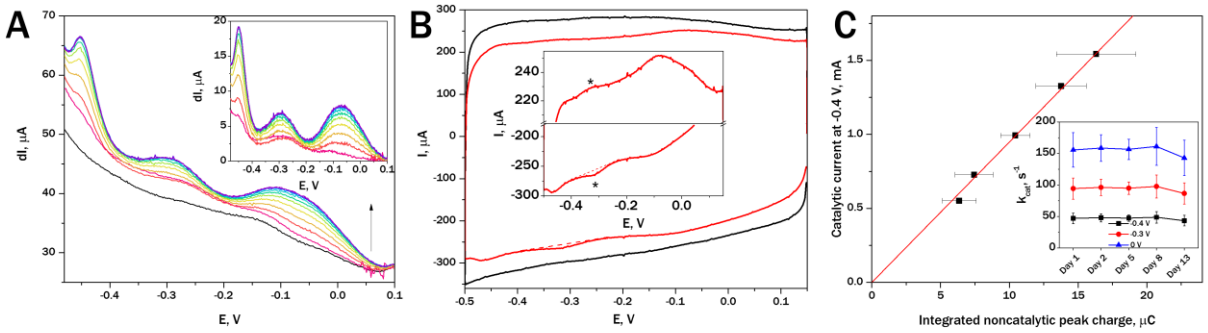
A
dI, μA
E, V
B
I, μA
E, V
C
Catalytic current at -0.4 V, mA
Integrated noncatalytic peak charge, μC
Day 1
Day 3
Day 5
Day 8
Day 13
-0.4 V
-0.3 V
0 V

Figure 8